

Article

Properties of Halide Perovskite Photodetectors with Little Rubidium Incorporation

Yuan-Wen Hsiao ¹, Jyun-You Song ¹, Hsuan-Ta Wu ², Ching-Chich Leu ^{3,*} and Chuan-Feng Shih ^{1,4,*}

¹ Department of Electrical Engineering, National Cheng Kung University, Tainan 70101, Taiwan; n28064012@mail.ncku.edu.tw (Y.-W.H.); c2781130@gmail.com (J.-Y.S.)

² Department and Institute of Electrical Engineering, Minghsin University of Science and Technology, Hsinchu 30401, Taiwan; htwu@must.edu.tw

³ Department of Chemical and Materials Engineering, National University of Kaohsiung, Kaohsiung 81148, Taiwan

⁴ Hierarchical Green-Energy Materials (Hi-GEM) Research Center, National Cheng Kung University, Tainan 70101, Taiwan

* Correspondence: ccleu@nuk.edu.tw (C.-C.L.); cfshih@mail.ncku.edu.tw (C.-F.S.); Tel.: +886-7-5919456 (ext. 7456) (C.-C.L.); +886-6-2757575 (ext. 62398) (C.-F.S.)

Abstract: This study investigates the effects of Rb doping on the Rb-formamidinium-methylammonium-PbI₃ based perovskite photodetectors. Rb was incorporated in the perovskite films with different contents, and the corresponding photo-response properties were studied. Doping of few Rb (~2.5%) was found to greatly increase the grain size and the absorbance of the perovskite. However, when the Rb content was greater than 2.5%, clustering of the Rb-rich phases emerged, the band gap decreased, and additional absorption band edge was found. The excess Rb-rich phases were the main cause that degraded the performance of the photodetectors. By space charge limit current analyses, the Rb was found to passivate the defects in the perovskite, lowering the leakage current and reducing the trap densities of carriers. This fact was used to explain the increase in the detectivity. To clarify the effect of Rb, the photovoltaic properties were measured. Similarly, a perovskite with 2.5% Rb doping increased the short-circuit current, revealing the decline of the internal defects. The 2.5% Rb doped photodetector showed the best performance with responsivity of 0.28 AW⁻¹ and ~50% quantum efficiency. Detectivity as high as 4.6 × 10¹¹ Jones was obtained, owing to the improved crystallinity and reduced defects.

Keywords: Rb doping; perovskite; photodetector; detectivity



Citation: Hsiao, Y.-W.; Song, J.-Y.; Wu, H.-T.; Leu, C.-C.; Shih, C.-F. Properties of Halide Perovskite Photodetectors with Little Rubidium Incorporation. *Nanomaterials* **2022**, *12*, 157. <https://doi.org/10.3390/nano12010157>

Academic Editor: Sofia Masi

Received: 26 November 2021

Accepted: 30 December 2021

Published: 3 January 2022

Publisher's Note: MDPI stays neutral with regard to jurisdictional claims in published maps and institutional affiliations.



Copyright: © 2022 by the authors. Licensee MDPI, Basel, Switzerland. This article is an open access article distributed under the terms and conditions of the Creative Commons Attribution (CC BY) license (<https://creativecommons.org/licenses/by/4.0/>).

1. Introduction

Organic perovskites have become the most important candidate in the future of high-efficiency solar cells because of easy fabrication, high absorption coefficient, wide band gap range, and fast charge transport [1]. As a hybrid organic-inorganic material, the crystalline properties and direct band gap characteristics mean that perovskites have different optoelectronic properties to the inorganic materials. The halide perovskites are defined by the formula AMX₃ [2], which is composed by a monovalent cation, A = formamidinium (H₂NCHNH₂⁺, FA) and methylammonium (CH₃NH₃⁺, MA); a divalent metal M from group II; and a halide anion X [3]. When the octahedral anions in the A sites were replaced by the inorganic cations such as cesium (Cs⁺) and rubidium (Rb⁺), the hybrid metal halide perovskites became more stable [4]. Various successful reports have used the alkaline stabilized perovskite for solar cells [5], lasers [6], and light-emitting diodes applications [7].

Recently, perovskite photodetectors (PDs) have been shown to have potential for light detection from visible to near infrared. Adjusting the structure by A-site doping improves the overall performance of the photodetector, resulting in high responsivity, low noise and fast response. For example, MA lead-halide-based PDs exhibited high detectivity, low

noise, and large linear dynamic range. However, it is very unstable at high temperature. Additionally, the quantum efficiency of the (MA⁺) perovskite based PDs is low [8–11]. FA⁺ perovskite improves the thermal stability, but the yellow δ -phase usually emerged that seriously degrades the properties. Stability of the perovskite can be improved by using mixing cations [12]. These kind of devices have better performance than the single and double-cation ones and better stability [13–15]. For example, we have demonstrated the FA-MA-Cs mixed perovskite PDs have superior behaviors than the FA-MA PDs [16]. Snaith et al. have reported that the FA-Cs mixed cationic perovskite film can be stable at a temperature above 100 °C [17]. Rb is also an element of group I, which has been reported to reduce the non-perovskite phase [18–20]. To our best knowledge, the influences of Rb doping on the performance of FAMAPbI₃ PDs has not been studied. In this work, the Rb-doped organic perovskite PDs were investigated. The Rb-doped PDs demonstrated a wide spectrum coverage in the visible range that has a maximum external quantum efficiency (EQE) of ~50%.

2. Materials and Methods

Rb_x(FA_{0.75}MA_{0.25})_{1-x}PbI₃ precursor solution was made by dissolving methylammonium (MA) iodide, formamidinium (FA) iodide, and lead iodide with 0.8 mL dimethylformamide (DMF) and 0.2 mL of dimethyl sulfoxide. The concentration of the perovskite precursor solution was 1.2 M. The solution was stirred until it was completely dissolved to form FA_{0.75}MA_{0.25}PbI₃ perovskite precursor solution. Rubidium iodide was pre-dissolved in dimethyl sulfoxide with a molar concentration of 1.5 M and then added to form the Rb_x(FA_{0.75}MA_{0.25})_{1-x} perovskite precursor, in which $x = 0, 0.025, 0.05, \text{ and } 0.075$. The indium tin oxide (ITO) glass was treated by acetone, isopropyl alcohol, and distilled water before coating. Then, it was dried with nitrogen and ultraviolet light ozone treated for 20 min. The perovskite precursor solution was spin-casted on ITO substrate. 200 μ L anti-solvents of chlorobenzene (CB) was dropped at the last 15 s, and then annealed at 50 °C for 20 min then heated up to 100 °C for 1 h.

The stacking sequence of the photodetector was ITO/PEDOT:PSS/perovskite/PC₆₁BM/BCP/Al. The PEDOT:PSS layer was coated on ITO-glass firstly. The perovskite thin film was spin-coated on the PEDOT:PSS layer by one-step method. The PC₆₁BM([6,6]-phenyl C₆₁butyric acid methyl ester) solutions was prepared by dissolving 20 mg PC₆₁BM powder in 1 mL chlorobenzene, continuously stirring for >12 h to ensure the full dissolution. PC₆₁BM solution was spin-coated at 3000 rpm for 40 s. Bathocuproine (BCP) was coated on the PCBM as the buffer layer. A 150 nm-thick Al electrode was thermally evaporated using a shadow mask. The structure of the PD device was plotted in Figure S1.

The microstructure and elementary mapping of the perovskite thin films were analyzed by scanning electron microscope (SEM, Hitachi SU8000, Tokyo, Japan) with energy dispersive X-ray spectroscopy (EDS, Bruker X-flash FlatQuad 5060FQ, Berlin, Germany). The crystalline structures were characterized by X-ray diffraction (XRD, Bruker D8 Discover, Karlsruhe, Germany). The steady-state photoluminescence (PL) spectra were collected by Horiba Jobin Yvon LabRAM HR system (Kyoto, Japan). The absorption spectrum of perovskite thin film was collected by using a HITACHI U4100 UV-vis-NIR spectrometer (Tokyo, Japan). The space-charge limit current (SCLC) was analyzed by current-voltage (I-V) measurement using Agilent E5270B in the dark. White light-emitting diode (300 lm, 10 Hz) was used to measure the photo-response, and solar simulator (AM 1.5, 100 mW/cm²) was used to measure the solar cells. The photocurrent was acquired using a Tektronix TBS-1104 digital oscilloscope (Beaverton, OR, USA).

3. Results

Figure 1a–d shows the morphologies of the perovskite films with 0%, 2.5%, 5% and 7.5% Rb, respectively. The grain size was estimated in the insets, increasing with the Rb content. Besides, the grain size distribution was much improved by 2.5–5% Rb doping, as compared with the pure (FA_{0.75}MA_{0.25})_{1-x}PbI₃ film that small crystallites embedded. When

the Rb content was increased to 7.5%, the small crystallites emerged between larger grains. Because the large and uniform grain size have been reported to be key for enhancement of the charge transport in the perovskites [13,21], the small amount of Rb incorporation could be expected to improve the photovoltaic and photodetector devices behaviors. The increase in the grain size by Rb doping was related to the stress-relief of the perovskite phase that incorporates the small ionic radius of Rb [19].

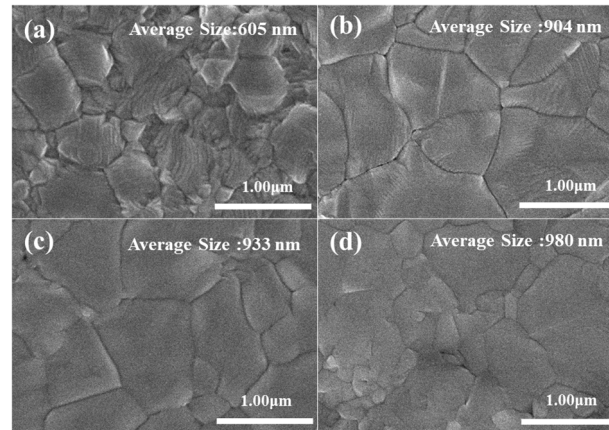


Figure 1. Top-view SEM morphology of Rb-doped (a) 0%, (b) 2.5%, (c) 5%, (d) 7.5% perovskite films.

The EDS elementary distribution of the Rb-doped films was shown in Figure 2 along with the clustering of Rb was found when the Rb concentration is higher than 2.5%, becoming more obvious when the doped Rb concentration reached 5% and 7.5%. The XRD patterns of the $\text{Rb}_x(\text{FA}_{0.75}\text{MA}_{0.25})_{1-x}\text{PbI}_3$ were shown in Figure 3. All of the diffraction peaks were associated with the planes of perovskites. The δ -FAPbI₃ s phase was observed in the 0% Rb sample, but was absent when 2% Rb was added to the perovskite films. The photo-inactive yellow phase δ -FAPbI₃ was almost eliminated by adding a moderate amount of Rb. Furthermore, PbI₂ precipitation that usually precipitates at grain boundaries was also suppressed by 2% Rb doping. However, the RbPbI₃ phase was found in the 5% and 7.5% Rb-doped samples that decreased the diffraction intensity. Figure 3b demonstrates the normalized PL peaks. The PL intensity increased by 2.5% Rb doping and the peaks red shift when the Rb content was increased, indicating a decrease in the band gap. This was ascribed to the Varshni shift that caused the band gap narrowing with the increase in the grain size [22]. Similar redshift upon RbI doping has been reported [23]. The PL intensity was slightly decreased by 2.5% Rb doping, but was markedly reduced by 5% and 7.5% Rb doping. This trend was similar with the variation of XRD intensity, therefore the mechanism was ascribed to the appearance of the yellow phase. Figure 3c shows the ultra-violet to red absorption spectra (400–650 nm) of the films. However, additional absorption edge was found around 430 nm for the 5% and 7.5% Rb doped samples. This is caused by the RbPbI₃ that has a larger band gap (2.7 eV) than $\text{FA}_{0.75}\text{MA}_{0.25}\text{PbI}_3$ (~1.55 eV) [24]. Due to the Rb-rich clusters, the 7.5% Rb-doped perovskite film showed the worst absorbance. A red shift caused by Rb doping in $\text{FA}_{0.75}\text{MA}_{0.25}\text{PbI}_3$ was obtained in the absorption spectrum, in good agreement with the PL result.

In order to study the defect behavior for the Rb-doped perovskite, the SCLC device was fabricated and the density of defects and trap states can be calculated by the SCLC model. Figure 4 demonstrates the dark J-V curves, in which three regions with different slopes that corresponded to the linear ohmic region ($J \propto V^n$, $n = 1$) at low bias, trap-filling limited region ($J \propto V^n$, $n > 3$) at middle bias, and a SCLC or Child's region ($J \propto V^n$, $n = 2$) at high bias were found and fitted linearly. The trap densities (N_t) of the electron-only devices were calculated [21]. The trap-filling limited voltage V_{TFL} can be determined by the onset of trap-filling limited region, and then the N_t can be derived. The linear fitting of different regions was shown in the figure based on the equation, $V_{\text{TFL}} = (q * N_t * d^2) /$

$(2 * \epsilon * \epsilon_0)$, where q , N_t , d , ϵ and ϵ_0 are electronic charge, trap density, the thickness of device, the dielectric constant of perovskite and the permittivity of free space, respectively. The dielectric constant used here was derived by measuring parallel capacitance of the perovskite using the structure of Ag/silicon/SiO₂/perovskite/Ag. The capacitance of native oxide Ag/silicon/SiO₂/Ag was firstly measured as a reference. As a result, the Rb-doped films had a lower V_{TFL} of 0.33 V and trap densities $6.55 \times 10^{15} \text{ cm}^{-3}$ than FA_{0.75}MA_{0.25}PbI₃ (0.42 V, $1.17 \times 10^{16} \text{ cm}^{-3}$).

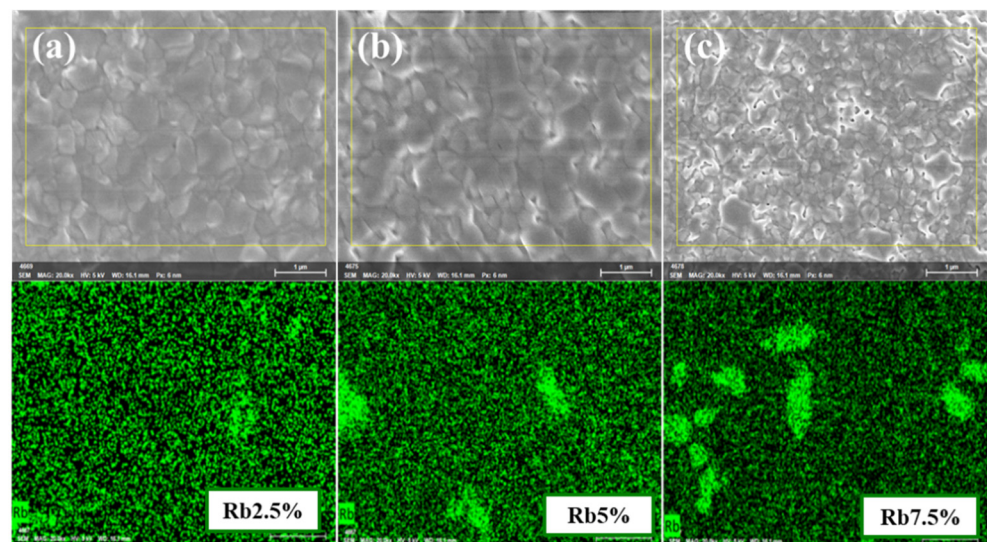


Figure 2. EDS mapping of Rb_x(FA_{0.75}MA_{0.25})_{1-x}PbI₃ with $x =$ (a) 2.5% (b) 5% (c) 7.5% Rb, respectively.

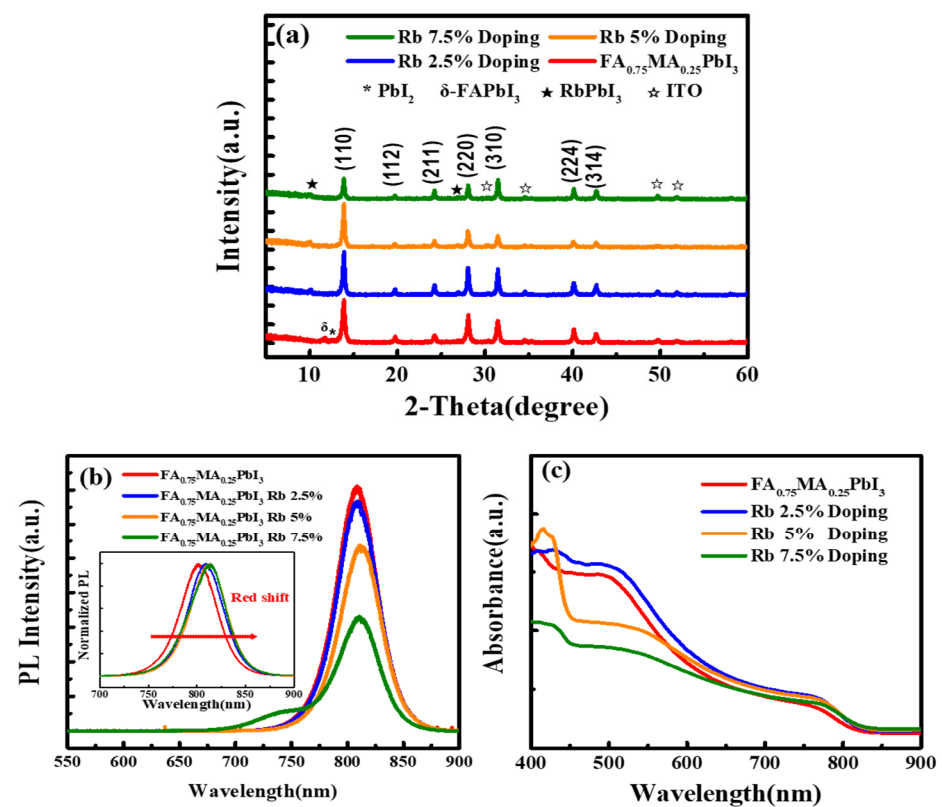


Figure 3. (a) XRD θ - 2θ , (b) PL spectra, and (c) Absorbance of Rb_x(FA_{0.75}MA_{0.25})_{1-x}PbI₃ films with $x = 0\%$, 2.5%, 5%, 7.5% Rb-doped, respectively.

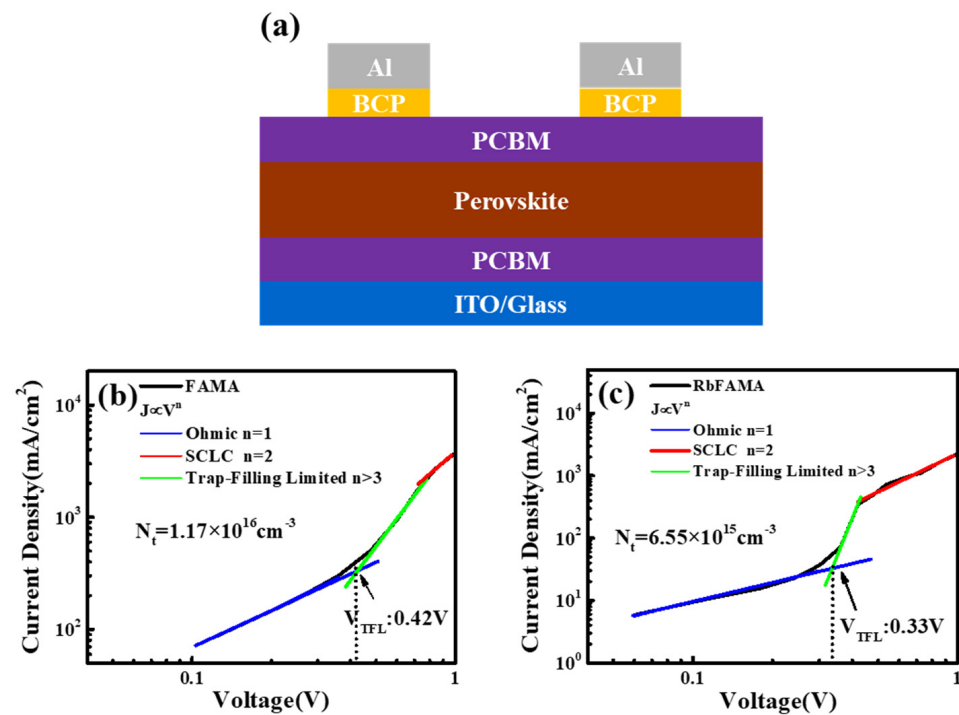


Figure 4. (a) SCLC device structure; (b) J-V relationship of $\text{FA}_{0.75}\text{MA}_{0.25}\text{PbI}_3$, and; (c) J-V relationship of $\text{Rb}_{0.025}\text{FA}_{0.75}\text{MA}_{0.25}\text{PbI}_3$. Trap-filling limit voltage (V_{TFL}) was determined from the linear fitting in trap-filling region (green) and trap density (N_t) was calculated accordingly.

Next, the influence of Rb^+ doping concentration on the photodetector performance are discussed. The continuous light response was shown in Figure 5, and the periodic switching characteristics were clearly observed. A continuous light response at a microsecond speed was observed. The doping of Rb caused an increase in the response time. The reason is that the phase separation of Rb-rich phases leads to a decrease in the crystalline properties of the film, which hinders carrier transfer behaviors. Differently, the response time of 7.5% Rb-doped films was the lowest among all of the Rb-doped samples. It was ascribed to the increase in the grain size. According to the literature, the larger crystal grains have lower bulk defects and higher carrier mobility, speeding up the response time [25].

Figure 6 shows the measured response time, spectral responsivity (R), noise current, EQE, and detectivity (D) of the PDs with various Rb. The EQE of the perovskite films was shown in Figure 6a. The 2.5% Rb-doped perovskite film had a highest EQE of $\sim 50\%$. The enhancement of the EQE spectrum was caused by the increased absorption of the perovskite. The EQE spectra were further used to represent the R (Figure 6b) [26]. Because of the proportion relationship between EQE and R, the 2.5% Rb-doped perovskite film also demonstrated the highest R of 0.273A/W . Figure 6c demonstrated the dark current (I_D) of the perovskite films. All of the Rb-doped showed lower leakage current compared with the undoped samples. Additionally, the 2.5% Rb-doped perovskite film had the lowest dark current. Detectivity of a PD can be determined from the I_D and R [26]. Figure 6d shows the relationship of D versus wavelengths. It was found that the detectivity was obviously increased by Rb doping for all of the Rb-doped films. Among these samples, the 2.5% Rb-doped PD showed the highest D (4.58×10^{11} Jones). The results revealed that the incorporation of Rb was mainly on the improvement of the detectivity, owing to the reduced internal defects and increased grain size and thin-film quality. Compared with the effect of Cs doping in the perovskite PDs, the Cs-doped PDs showed marked reduction in the response time but the change in the rise time and fall time of the Rb-doped PDs is not obvious [27]. The appearance of Rb-rich second phase should be responsible for this difference.

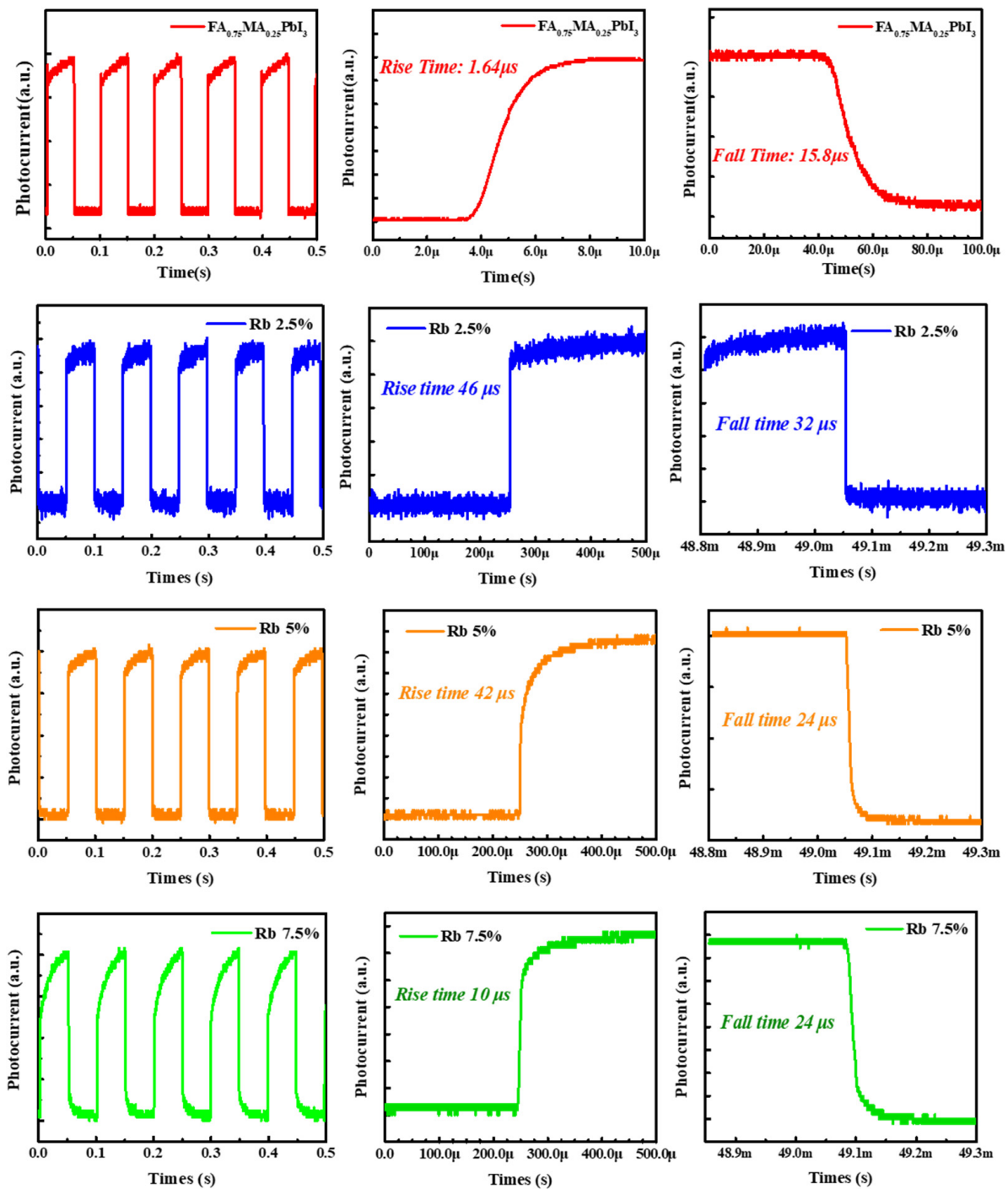


Figure 5. Cyclic photoresponse with time of perovskite FA_{0.75}MA_{0.25}PbI₃ photodetectors with different Rb⁺ doping concentration of 0%, 2.5%, 5%, 7.5% Rb, and magnification in rise side and fall side, respectively.

The solar cell parameters were measured and shown in Figure S2 to further understand the photo-response mechanism of the Rb-doped PDs. The light source was an AM1.5G solar simulator. Similarly, 2.5% Rb⁺ doped solar cells had an increase in the conversion efficiency when it was compared with the undoped one, mainly caused by the great increase in the J_{sc}. It is believed that the improvement of the J_{sc} was related to the decline of the trap densities and improved crystal quality, caused by the incorporation of Rb that inhibited the formation of δ-FAPbI₃ phases and internal defects.

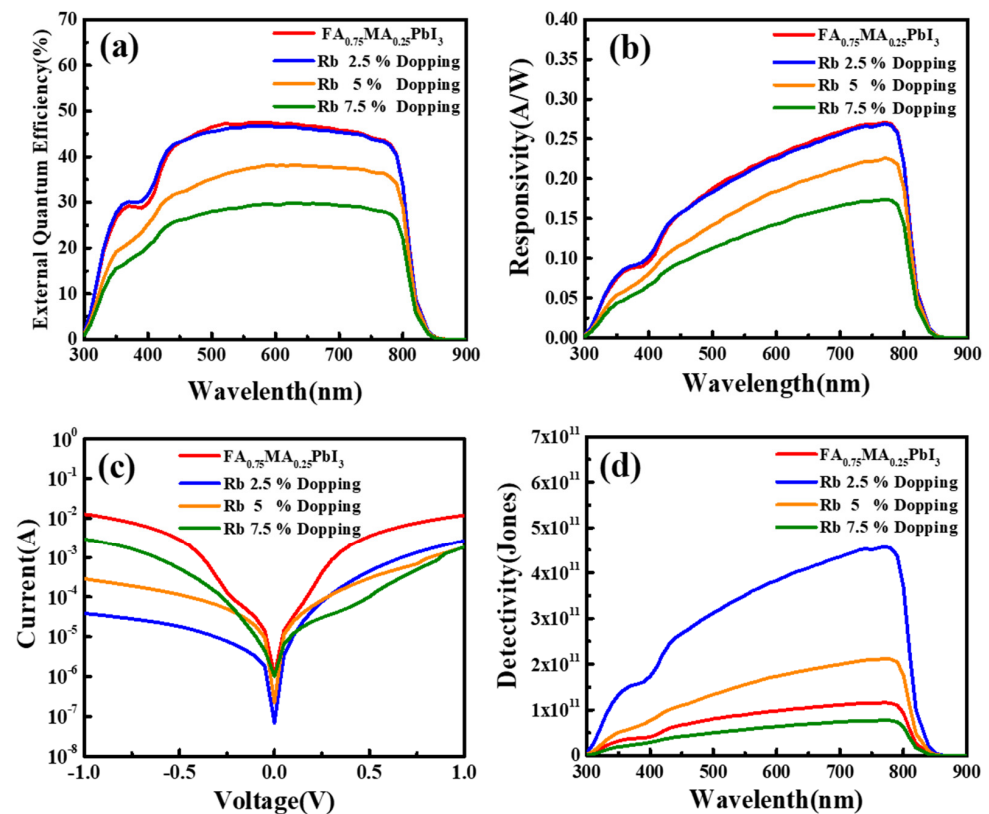


Figure 6. (a) EQE spectra, (b) responsivity, (c) I-V relationship without light, and (d) detectivity of perovskite PDs with various Rb contents.

4. Conclusions

The impacts of Rb doping on the organic perovskite PDs was investigated. It was found that slight addition of the Rb with 2.5% Rb increased the grain size, reducing the unwanted yellow phase. The lattice expansion was observed by XRD that shows monotonically shift of peaks toward higher angle when the Rb contents was increased. As a result, the red shift in PL and absorption spectra was observed by increasing Rb. SEM images shows that when the Rb concentration is higher than 2.5%, the Rb-rich cluster emerged. For the PD performance, the rise time and fall time changed little, but the detectivity was markedly enhanced owing to the reduction of the dark current by Rb doping. By SCLC analysis, the Rb doping was found to have passivated the defects in the perovskite, lowering the leakage current and reducing the trap densities of carriers.

Supplementary Materials: The following supporting information can be downloaded at: <https://www.mdpi.com/article/10.3390/nano12010157/s1>, Figure S1: Device structure of perovskite photodetectors. Figure S2: Parameters of solar cells of Rb-doped $\text{Rb}_x(\text{FA}_{0.75}\text{MA}_{0.25}\text{PbI}_3)_{1-x}$ solar cells.

Author Contributions: Conceptualization, Y.-W.H., J.-Y.S. and C.-F.S.; Data curation, Y.-W.H.; Formal analysis, H.-T.W.; Investigation, H.-T.W.; Methodology, Y.-W.H. and J.-Y.S.; Validation, Y.-W.H. and J.-Y.S.; Writing—original draft, Y.-W.H. and C.-F.S.; Writing—review and editing, Y.-W.H., C.-C.L. and C.-F.S. All authors have read and agreed to the published version of the manuscript.

Funding: This research received no external funding.

Institutional Review Board Statement: Not applicable.

Informed Consent Statement: Not applicable.

Data Availability Statement: Data is contained within the article or supplementary material.

Acknowledgments: The authors are thankful for the support of the Ministry of Science and Technology of the Republic of China under Contract No. (MOST 110-2224-E-006-006) and Taiwan Semiconductor Research Institute (JDP110-Y1-021). The authors would like to thank Hui-Jung Shih with the Core Facility Center of National Cheng Kung University for supporting the use of HR-SEM (Hitachi SU8000) and BRUKER XFlash 5010. Additionally, this work was also grateful by the Hierarchical Green-Energy Materials (Hi-GEM) Research Center supported, within the Higher Education Sprout Project of the Ministry of Education (MOST 110-2634-F-006 -017) in Taiwan.

Conflicts of Interest: The authors declare no conflict of interest.

References

1. Tan, H.; Che, F.; Wei, M.; Zhao, Y.; Saidaminov, M.I.; Todorović, P.; Broberg, D.; Walters, G.; Tan, F.; Zhuang, T.; et al. Dipolar cations confer defect tolerance in wide-bandgap metal halide perovskites. *Nat. Commun.* **2018**, *9*, 3100. [\[CrossRef\]](#)
2. Saliba, M.; Matsui, T.; Domanski, K.; Seo, J.-Y.; Ummadisingu, A.; Zakeeruddin, S.M.; Correa-Baena, J.-P.; Tress, W.R.; Abate, A.; Hagfeldt, A.; et al. Incorporation of rubidium cations into perovskite solar cells improves photovoltaic performance. *Science* **2016**, *354*, 206–209. [\[CrossRef\]](#)
3. Yao, F.; Gui, P.; Zhang, Q.; Lin, Q. Molecular engineering of perovskite photodetectors: Recent advances in materials and devices. *Mol. Syst. Des. Eng.* **2018**, *3*, 702–716. [\[CrossRef\]](#)
4. Lin, Q.; Armin, A.; Nagiri, R.; Burn, P.; Meredith, P. Electro-optics of perovskite solar cells. *Nat. Photonics* **2015**, *9*, 106–112. [\[CrossRef\]](#)
5. Liu, X.; Zhang, Y.; Shi, L.; Liu, Z.; Huang, J.; Yun, J.S.; Zeng, Y.; Pu, A.; Sun, K.; Hameiri, Z.; et al. Exploring Inorganic Binary Alkaline Halide to Passivate Defects in Low-Temperature-Processed Planar-Structure Hybrid Perovskite Solar Cells. *Adv. Energy Mater.* **2018**, *8*, 1800138. [\[CrossRef\]](#)
6. Jia, Y.; Kerner, R.A.; Grede, A.J.; Rand, B.P.; Giebink, N.C. Continuous-wave lasing in an organic–inorganic lead halide perovskite semiconductor. *Nat. Photonics* **2017**, *11*, 784–788. [\[CrossRef\]](#)
7. Cao, Y.; Wang, N.; Tian, H.; Guo, J.; Wei, Y.; Chen, H.; Miao, Y.; Zou, W.; Pan, K.; He, Y.; et al. Perovskite light-emitting diodes based on spontaneously formed submicrometre-scale structures. *Nature* **2018**, *562*, 249–253. [\[CrossRef\]](#) [\[PubMed\]](#)
8. Cao, F.; Meng, L.; Wang, M.; Tian, W.; Li, L. Gradient Energy Band Driven High-Performance Self-Powered Perovskite/CdS Photodetector. *Adv. Mater.* **2019**, *31*, e1806725. (In English) [\[CrossRef\]](#) [\[PubMed\]](#)
9. Li, J.; Yuan, S.; Tang, G.; Li, G.; Liu, D.; Li, J.; Hu, X.; Liu, Y.; Li, J.; Yang, Z.; et al. High-Performance, Self-Powered Photodetectors Based on Perovskite and Graphene. *ACS Appl. Mater. Interfaces* **2017**, *9*, 42779–42787. [\[CrossRef\]](#)
10. Zhou, H.; Mei, J.; Xue, M.; Song, Z.; Wang, H. High-Stability, Self-Powered Perovskite Photodetector Based on a CH₃NH₃PbI₃/GaN Heterojunction with C₆₀ as an Electron Transport Layer. *J. Phys. Chem. C* **2017**, *121*, 21541–21545. [\[CrossRef\]](#)
11. Ghosh, J.; Natu, G.; Giri, P. Plasmonic hole-transport-layer enabled self-powered hybrid perovskite photodetector using a modified perovskite deposition method in ambient air. *Org. Electron.* **2019**, *71*, 175–184. [\[CrossRef\]](#)
12. Wang, M.; Jiang, X.; Bian, J.; Feng, Y.; Wang, C.; Huang, Y.; Zhang, Y.; Shi, Y. High-Performance and Stable Mesoporous Perovskite Solar Cells via Well-Crystallized FA_{0.85}MA_{0.15}Pb(I_{0.8}Br_{0.2})₃. *ACS Appl. Mater. Interfaces* **2018**, *11*, 2989–2996. [\[CrossRef\]](#)
13. Singh, T.; Miyasaka, T. Stabilizing the Efficiency Beyond 20% with a Mixed Cation Perovskite Solar Cell Fabricated in Ambient Air under Controlled Humidity. *Adv. Energy Mater.* **2017**, *8*, 1700677. [\[CrossRef\]](#)
14. Wang, Y.; Wu, J.; Zhang, P.; Liu, D.; Zhang, T.; Ji, L.; Gu, X.; Chen, Z.D.; Li, S. Stitching triple cation perovskite by a mixed anti-solvent process for high performance perovskite solar cells. *Nano Energy* **2017**, *39*, 616–625. [\[CrossRef\]](#)
15. Eze, V.O.; Seike, Y.; Mori, T. Efficient planar perovskite solar cells using solution-processed amorphous WO_x/fullerene C₆₀ as electron extraction layers. *Org. Electron.* **2017**, *46*, 253–262. [\[CrossRef\]](#)
16. Adams, G.R.; Eze, V.O.; Shohag, A.S.; Simpson, R.; Parker, H.; I Okoli, O. Fabrication of rapid response self-powered photodetector using solution-processed triple cation lead-halide perovskite. *Eng. Res. Express* **2020**, *2*, 015043. [\[CrossRef\]](#)
17. McMeekin, D.P.; Sadoughi, G.; Rehman, W.; Eperon, G.E.; Saliba, M.; Hörantner, M.T.; Haghighirad, A.; Sakai, N.; Korte, L.; Rech, B.; et al. A mixed-cation lead mixed-halide perovskite absorber for tandem solar cells. *Science* **2016**, *351*, 151–155. [\[CrossRef\]](#)
18. Sa, R.; Liu, M.; Zha, W. Effect of rubidium incorporation on the structural, electronic and properties of MAPbI₃. *Chem. Phys. Lett.* **2020**, *743*, 137179. [\[CrossRef\]](#)
19. Erodici, M.P.; Pierone, P.J.; Hartono, N.T.P.; Hidalgo, J.; Lai, B.; Buonassisi, T.; Correa-Baena, J.-P.; Sher, M.-J. Enhanced charge carrier lifetime and mobility as a result of Rb and Cs incorporation in hybrid perovskite. *Appl. Phys. Lett.* **2021**, *118*, 063901. [\[CrossRef\]](#)
20. Binyamin, T.; Pedesseau, L.; Remennik, S.; Sawahreh, A.; Even, J.; Etgar, L. Fully Inorganic Mixed Cation Lead Halide Perovskite Nanoparticles: A Study at the Atomic Level. *Chem. Mater.* **2019**, *32*, 1467–1474. [\[CrossRef\]](#)
21. Shi, D.; Adinolfi, V.; Comin, R.; Yuan, M.; Alarousu, E.; Buin, A.; Chen, Y.; Hoogland, S.; Rothenberger, A.; Katsiev, K.; et al. Low trap-state density and long carrier diffusion in organolead trihalide perovskite single crystals. *Science* **2015**, *347*, 519–522. [\[CrossRef\]](#)
22. Duong, T.; Mulmudi, H.K.; Shen, H.; Wu, Y.; Barugkin, C.; Mayon, Y.O.; Nguyen, H.T.; Macdonald, D.; Peng, J.; Lockrey, M.; et al. Structural engineering using rubidium iodide as a dopant under excess lead iodide conditions for high efficiency and stable perovskites. *Nano Energy* **2016**, *30*, 330–340. [\[CrossRef\]](#)
23. D’Innocenzo, V.; Kandada, A.R.S.; De Bastiani, M.; Gandini, M.; Petrozza, A. Tuning the Light Emission Properties by Band Gap Engineering in Hybrid Lead Halide Perovskite. *J. Am. Chem. Soc.* **2014**, *136*, 17730–17733. [\[CrossRef\]](#)

24. Park, Y.H.; Jeong, I.; Bae, S.; Son, H.J.; Lee, P.; Lee, J.; Lee, C.-H.; Ko, M.J. Inorganic Rubidium Cation as an Enhancer for Photovoltaic Performance and Moisture Stability of $\text{HC}(\text{NH}_2)_2\text{PbI}_3$ Perovskite Solar Cells. *Adv. Funct. Mater.* **2017**, *27*, 1605988. [[CrossRef](#)]
25. Tong, S.; Wu, H.; Zhang, C.; Li, S.; Wang, C.; Shen, J.; Xiao, S.; He, J.; Yang, J.; Sun, J.; et al. Large-area and high-performance $\text{CH}_3\text{NH}_3\text{PbI}_3$ perovskite photodetectors fabricated via doctor blading in ambient condition. *Org. Electron.* **2017**, *49*, 347–354. [[CrossRef](#)]
26. Hun, C.-M.; Tien, C.-H.; Lee, K.-L.; Lai, H.-Y.; Chen, L.-C. The Effects of Temperature on the Growth of a Lead-Free Perovskite-Like $(\text{CH}_3\text{NH}_3)_3\text{Sb}_2\text{Br}_9$ Single Crystal for An MSM Photodetector Application. *Sensors* **2021**, *21*, 4475. [[CrossRef](#)]
27. Hsiao, Y.-W.; Song, J.-Y.; Wu, H.-T.; Hong, K.-T.; Leu, C.-C.; Shih, C.-F. Effects of cesium content on the triple-cation lead halide perovskite photodetectors with enhanced detectivity and response time. *J. Alloy. Compd.* **2021**, *889*, 161621. [[CrossRef](#)]